Letter

Propagation, dissipation, and breakdown in quantum anomalous Hall edge states probed by microwave edge plasmons

Torsten Röper,[1] Hugo Thomas,[1] Daniel Rosenbach,[1] Anjana Uday,[1] Gertjan Lippertz,[1] Anne Denis,[2] Pascal Morfin,[2] Alexey A. Taskin,[1] Yoichi Ando,[1] and Erwann Bocquillon[1,*]

[1]*II. Physikalisches Institut, Universität zu Köln, Zülpicher Strasse 77, D-50937 Köln, Germany*

[2]*Laboratoire de Physique de l'Ecole Normale Supérieure, ENS, Université PSL, CNRS, Sorbonne Université, Université de Paris, F-75005 Paris, France*

(Received 31 May 2024; revised 1 August 2024; accepted 26 August 2024; published 7 October 2024)

The quantum anomalous Hall (QAH) effect, with its single chiral, topologically protected edge state, offers a platform for flying Majorana states as well as nonreciprocal microwave devices. While recent research showed the nonreciprocity of edge plasmons in Cr-doped $(Bi_xSb_{1-x})_2Te_3$, the understanding of their dissipation remains incomplete. Our study explores edge plasmon dissipation in V-doped $(Bi_xSb_{1-x})_2Te_3$ films, analyzing microwave transmission across various conditions. We identify interactions with charge puddles as a primary source, providing insights critical for developing improved QAH-based technologies.

DOI: 10.1103/PhysRevB.110.L161403

Introduction. Magnetic topological insulators exhibit the quantum anomalous Hall (QAH) effect [1–3], namely, the occurrence of a single chiral edge state, carrying current in a direction determined by the material's magnetization direction, while the bulk remains insulating. Despite magnetic and electronic disorder, quantized dissipationless edge transport is observed in the absence of a magnetic field at very low temperatures. This robust topological phase of matter opens interesting perspectives for quantum metrology [4–7] and nonreciprocal microwave components [8,9]. When in proximity to a superconductor [10], these edge states allow for the creation of flying non-Abelian anyons, which can be braided as they propagate [11,12]. A pending issue is, in particular, the origin of the breakdown of the QAH regime at higher temperatures or larger currents, attributed to either heating effects [6,13] as in the quantum Hall effect [14] or a field-induced percolation of charge puddles created by disordered fluctuations of the Fermi level [15]. Prospective applications require a good understanding and control of the high-frequency propagation of plasmons in the edge state. To date, two studies have focused on narrow-band resonant geometries in Cr-doped $(Bi_xSb_{1-x})_2Te_3$ disks and reported a circulation effect in this material, with the first investigation of losses [9,16]. The screening and dissipation due to charge puddles deserve particular attention. Here, we report on a systematic and broadband study of plasmons in the QAH insulator V-doped $(Bi_xSb_{1-x})_2Te_3$ (V-BST), a material which offers better performance and a more stable QAH state in zero magnetic field owing to its larger coercive field ($\mu_0 H_c \simeq 0.9\,\mathrm{T}$) compared to Cr-doped BST ($\mu_0 H_c \simeq 0.2\,\mathrm{T}$) [1,4,6]. Using a microwave Hall bar geometry with capacitively coupled input and readout ports, we carry out broadband measurements from 0.3 to 4 GHz. We resolve the phase velocity and the dissipation of plasmons from the phase and amplitude of the transmission coefficient, respectively. We observe low-dissipation, high-frequency transport up to ~ 4 GHz and $\sim 100\,\mu\mathrm{m}$. We fully characterize the plasmon losses and observe a frequency-independent loss mechanism, which we correlate to the residual longitudinal resistance of the edge state, and a frequency-dependent dissipation, which we ascribe to the presence of charge puddles near the edge state.

Sample geometry and DC characterization. The studied devices are fabricated from 8 nm thick films of V-BST grown on InP (111)A substrates using molecular beam epitaxy, capped with a 4 nm layer of Al_2O_3. By optimizing the Bi:Sb ratio, the chemical potential is adjusted to reside within the magnetic exchange gap without the need for electrostatic gating. After patterning Ohmic contacts (5 nm Pt/45 nm Au), the V-BST mesa is wet-chemically etched. Capacitively coupled finger gates are realized with an additional 12 nm layer of Al_2O_3, as a gate dielectric and a metallic gate electrode (5 nm Pt/45 nm Au). Coplanar waveguides (5 nm Pt/45 nm Au) are added to guide microwave signals. Notably, our experimental setup excludes a top gate to prevent screening of edge plasmons, as discussed in [17]. Figure 1(a) shows a microscope image of one of the devices. Four samples were investigated with minor variations in the geometry (see an example measurement configuration in the Supplemental Material [18]), and each was measured in various configurations and for various path lengths. Thanks to Ohmic contacts on the device or on an adjacent Hall bar, the DC longitudinal and transverse (Hall) resistances are determined at a base temperature of $T \simeq 15\,\mathrm{mK}$ before rf measurements. All samples exhibit a quantized Hall resistance $R_{yx} = R_K = h/e^2$, with deviations

*Contact author: bocquillon@ph2.uni-koeln.de

Published by the American Physical Society under the terms of the Creative Commons Attribution 4.0 International license. Further distribution of this work must maintain attribution to the author(s) and the published article's title, journal citation, and DOI.

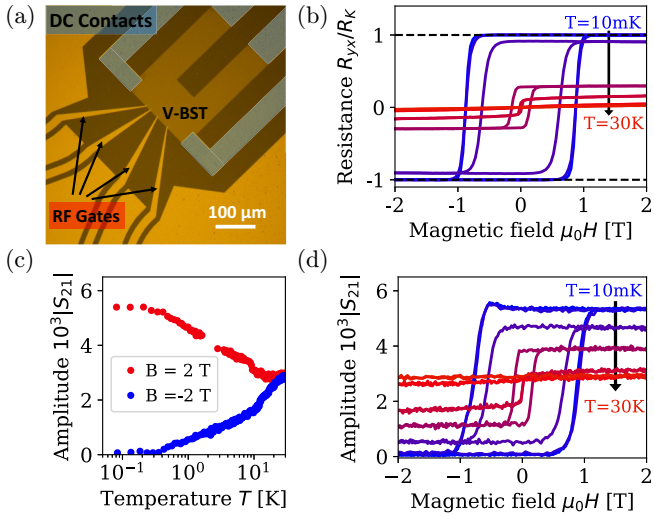


FIG. 1. Sample geometry, DC, and microwave measurements: (a) Optical microscope image of sample D. The π-shaped mesa (medium brown) is contacted via Ohmic contacts highlighted in blue for DC measurements of R_{xx} and R_{yx}. A set of four narrow rf gates allows for driving and reading out microwave signals in varying gate combinations, yielding the transmission coefficients S_{12} for different path lengths l. (b) Temperature-dependent field sweeps for the DC transversal resistance R_{yx}, which shows quantization until approximately 200 mK. The curves correspond to the following temperatures: $T = 0.01$, 0.3, 1, 3.5, 10, 20, and 30 K. (c) The amplitude for $\mu_0 H = \pm 2$ T as a function of temperature T ($L = 20\,\mu$m, $U \simeq 125\,\mu$V, $f \simeq 750$ MHz, device C). (d) The amplitude as a function of magnetic field $\mu_0 H$ for $L = 20\,\mu$m and $f = 1$ GHz on device C for the same temperatures as in (b).

of only a few percent (device B is of lower quality). However, the samples differ more strongly in their residual longitudinal resistance r_{xx}, ranging from 0.2 to 5.8 $\Omega\,\mu\text{m}^{-1}$ in zero field (calculated from the longitudinal R_{xx} measured along a distance of 80 µm between the Ohmic contacts). The low values of r_{xx} indicate that charge transport occurs mainly via the edge states and that bulk transport is suppressed. For clarity, we focus on data measured on device C in the rest of the main text. More data are shown in the Supplemental Material [18], with similar conclusions. The Hall resistance R_{yx} of device C is shown as a function of the out-of-plane magnetic field $\mu_0 H$ in Fig. 1(b) for various temperatures, revealing a well-known hysteretic pattern [1]. Following prior reports [15,19], quantization is visible until onset of bulk transport at approximately $T = 200$ mK, while the hysteresis remains visible until the Curie temperature (approximately 20 to 25 K depending on the sample).

Microwave setup and calibration. The microwave measurements are carried out using a vector network analyzer. The signal at the detection gate is amplified using a cryogenic amplifier (0.3–14 GHz, +38 dB). Nonresonant broadband detection methods require a challenging calibration, which we here briefly summarize (we refer the reader to the Supplemental material for details [18]). First, the absence of an isolator (to preserve the wide bandwidth of the amplifier) results in standing waves due to the large impedance mismatch between the microwave setup (50 Ω) and the sample ($R_K \simeq 25.8\,\text{k}\Omega$). Second, a large capacitive stray coupling between the injection and detection ports is observed, which can exceed the transmission via edge plasmons. To correct for stray coupling and other distortions within the setup, we measure reference configurations: (1) a dummy structure without a V-BST mesa serves to calibrate the stray coupling, and (2) a through line giving access to the phase shift accumulated along the measurement setup. The calibration of the phase is determined to be robust and device independent, with a typical accuracy < 0.2 rad for $f > 1$ GHz. The signal amplitude is more device dependent and suffers from a more inaccurate calibration. We estimate a systematic error of typically 20% in the same frequency range (see the Supplemental Material [18]). We will always refer to the corrected transmission coefficient S_{21} in the following. Due to the asymmetric device geometry, for negative magnetization, plasmons are strongly attenuated along the long edge path ($L > 2$ mm), and we expect to measure only stray signals. In this configuration, we observe that the signal measured on the device is very close to that of the dummy, validating our experimental approach. For the opposite magnetization direction, we observe a strong additional signal, attributed to edge state transport traveling on shorter distances ($L < 100\,\mu$m). Figure 1(d) shows the amplitude of the transmission as a function of the magnetic field $\mu_0 H$ for temperature values between 10 mK and 30 K, which evidences the hysteretic behavior of the transmission S_{21}, showing a high amplitude for positive magnetization ($L = 20\,\mu$m) and no or low signal for negative magnetization ($L > 2$ mm). Figure 1(c) shows the temperature dependence of the amplitude at $\mu_0 H = \pm 2$ T. A constant amplitude is observed upon warming until approximately 200 mK. Beyond this temperature range, the amplitude of the edge state signal at $\mu_0 H = +2$ T drops, while a finite and increasing amplitude is measured at $\mu_0 H = -2$ T. These two features mark the onset of bulk conductivity as reported in DC transport experiments [4,15]. Moreover, the coercive field is approximately 0.9 T at $T = 10$ mK and decreases with increasing temperature until the hysteresis vanishes at approximately 22 K. These observations in accordance with the DC characterization data shown in Fig. 1(b) confirm that, after proper calibration, the microwave transmission coefficient associated with transport through the edge state can be singled out.

Edge plasmon velocity. After investigating the amplitude of S_{21}, we now briefly analyze its phase to obtain an estimate of the velocity of edge plasmons, before presenting a circuit model describing both in a unified manner. After calibration, the phase shift $\phi = \arg(S_{21})$ depends on the velocity v and the propagation length L of the edge plasmon, as well as an additional contribution ϕ_g from the capacitive coupling between the finger gate and edge state (see the Supplemental Material [18]): $\phi(f) = 2\pi f L/v + \phi_g(f)$. The phase shift ϕ, after the phase at zero frequency is subtracted, is shown in Fig. 2(a) for the lengths of $L = 20$, 40, and 70 µm and for an amplitude $U \simeq 225\,\mu$V. The phase shift increases with increasing frequency f and length L, as expected. For each frequency f, a linear fit of ϕ as a function of L yields the slope $d\phi/dL = 2\pi f/v$ and the intercept ϕ_g [see example fits in Fig. 2(b)]. A second linear fit of $d\phi/dL$ as a function of f [Fig. 2(c)] yields a velocity of $v = 450 \pm 20\,\text{km s}^{-1}$. Similarly, the intercept ϕ_g is well fitted with a simple model of

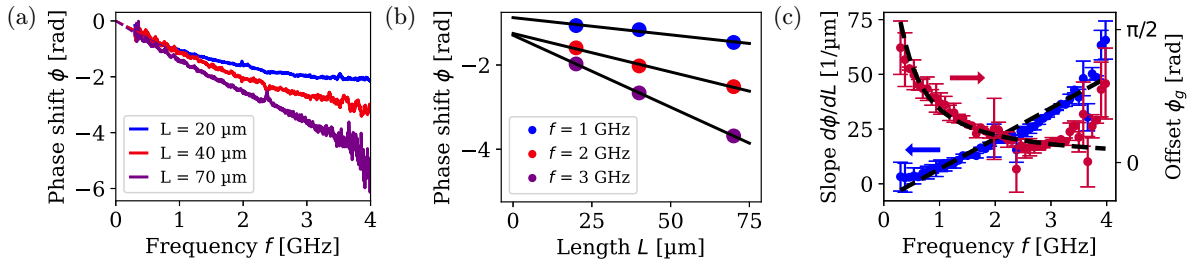


FIG. 2. Velocity of edge plasmons. (a) Phase shift as a function of frequency for a length L of 20, 40, and 70 µm for an excitation voltage of $U \simeq 225\,\mu\text{V}$ (device C). The dashed lines show linear fits for frequencies below 0.8 GHz, which we use to subtract the phase at zero frequency. (b) Length dependence of phase shift for a frequency of 1, 2, and 3 GHz. The black lines correspond to linear fits. (c) Slope $d\phi/dL$ and intercept ϕ_g as a function of frequency f. The slope is fitted with a linear function yielding a velocity of $v = 450 \pm 20\,\text{km s}^{-1}$, while the intercept ϕ_g is well fitted by a model of the gate coupling derived from [20], with a gate capacitance $C_g = 19 \pm 2\,\text{fF}$.

gate-edge coupling derived by Gourmelon *et al.* [20], yielding a gate capacitance of $C_g = 19 \pm 2\,\text{fF}$. Despite the uncertainty and inaccuracy in the calibration of multiple samples and configurations, the phase ϕ and its dependence on length L and frequency f are well captured by our simple assumptions, providing confidence in our analysis. The estimate of v is comparable to measurements of edge plasmons in Cr-doped BST [9,16] and close to the Fermi velocity measured by angle-resolved photoemission spectroscopy in related bulk compounds [21,22]. The velocity v is, however, lower than the velocity of quantum Hall edge states in ungated devices [23], where it is increased by electron-electron interaction within the edge state [24,25]. This could signal the screening of interactions by charge puddles created by fluctuations of the Fermi level, whose role has been exemplified in high-frequency transport of edge states in the quantum Hall and quantum spin Hall insulators [16,20,26]. In the following, we present an analysis of our results based on a circuit model describing the puddles.

Charge puddle circuit model. To treat propagation, dispersion, and dissipation on equal footing, we model our results using the circuit model shown in Fig. 3(a), adapted from Kumada *et al.* [27]. The edge state is modeled as a transmission line of impedance R_K and line capacitance c_e, corresponding to the quantum capacitance of the edge state [28]. The conductivity g_e models frequency-independent dissipation, which we will later confirm stems from the residual longitudinal resistance seen in DC transport experiments. The conductance g_p and the capacitance c_p model the interaction with charge puddles as an RC circuit, with characteristic frequency $f_p = g_p/(2\pi c_p)$, where the total capacitance c_p includes both the geometric and quantum capacitances [29,30]. The conductance g_p corresponds to the microwave conductance of the bulk. We find the following dispersion relation:

$$k(f) = 2\pi f R_K c_e - i R_K g_e + \frac{2\pi f R_K c_p}{1 + \frac{if}{f_p}}. \tag{1}$$

With these new circuit elements, the dispersion relation of edge plasmons is modified in two ways. First, charge puddles slow down edge plasmons, reducing the velocity from $1/R_K c_e$ to $1/R_K(c_e + c_p)$ (assuming the low-frequency limit $f \ll f_p$). Second, dissipation through puddles takes place, with $\text{Im}[k(f)] \propto f^2$, yielding the same expression as Martinez *et al.* [16]. To reduce the number of fit parameters, we assume that $c_e \ll c_p$, as observed in similar cases [20,31]. Additionally, we account for the capacitive coupling between the finger gate and the edge state by the capacitor C_g following Ref. [28].

Analysis and fit of the data. Figures 3(b) and 3(c) show the amplitude and phase of S_{21} as a function of frequency f for a distance $L = 20\,\mu\text{m}$ at different excitation voltages U, together with fits using the circuit model. We first discuss the fit for an excitation voltage $U \simeq 225\,\mu\text{V}$ [purple curve, same amplitude as in Fig. 2(a)]. The fit shows good agreement with the data ($R^2 = 0.98$). It yields a gate coupling capacitance $C_g = 24.4 \pm 0.2\,\text{fF}$ and a line capacitance $c_p = 102 \pm 2\,\text{pF m}^{-1}$, from which we derive the velocity $v = 380 \pm 3\,\text{km s}^{-1}$. The velocity v agrees with our earlier coarse estimate and

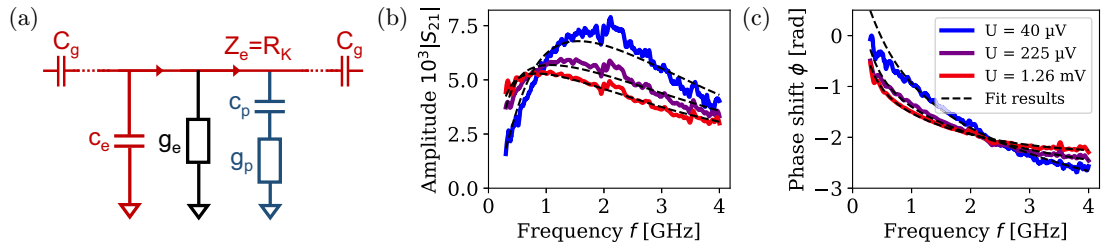


FIG. 3. Charge puddle model. (a) Circuit diagram, where the edge channel is described by a transmission line of impedance Z_e and a line capacitance of c_e that is coupled to the setup via a coupling capacitance C_g. The interaction with charge puddles is modeled by a conductivity g_e in DC and by a conductivity g_p and the line capacitance c_p for high frequencies. (b) and (c) Measurements (solid colored lines) and fits (dashed lines) of the amplitude $|S_{21}|$ and phase ϕ, respectively, in device C for $L = 20\,\mu\text{m}$, $T = 20\,\text{mK}$, and $\mu_0 H = 2\,\text{T}$.

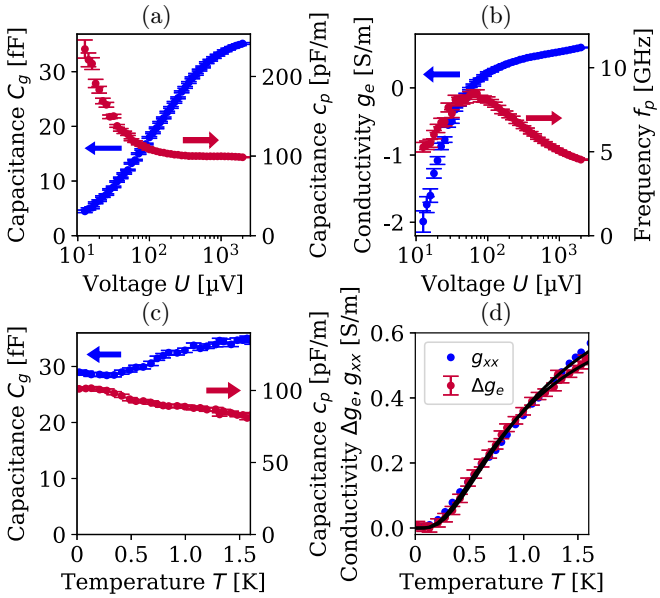


FIG. 4. Excitation voltage and temperature dependence of the fit parameter. (a) and (b) Results of the fit model for the frequency-dependent transmission at different voltages U. The coupling capacitance C_g and the conductivity g_e increase with the excitation voltage, while the puddle capacitance c_p decreases. All curves show a transition at an excitation voltage of $U \simeq 60\,\mu\text{V}$. (c) Temperature dependence of the fit parameter C_g and c_p for $U \simeq 125\,\mu\text{V}$. (d) Temperature dependence of the fitted conductivity g_e (red) and of the longitudinal conductance g_{xx} (blue), together with fits based on the variable range hopping model, yielding $T_0 = 17.4 \pm 0.6\,\text{K}$ and $T_0 = 15.4 \pm 0.2\,\text{K}$, respectively.

results obtained for Cr-doped BST [9,16]. The puddles show a characteristic frequency of $f_p = 7.0 \pm 0.1\,\text{GHz}$, in rough accordance with Ref. [32], in which the bulk microwave conductivity of similar compounds was studied. However, the estimate of the fit parameter g_e, which controls the amplitude of S_{21}, is subject to an overall uncertainty on the calibration of the amplitude, as outlined in the Supplemental Material [18], yielding unreliable absolute values. Hence, we will instead focus on relative changes in g_e. We note that the data for higher excitation voltages U are also well-fitted by our model, although for considerably different parameters. We discuss next the variations of the obtained parameters.

Dissipation of edge plasmons. We previously identified two distinct dissipation mechanisms in the edge state: (1) a frequency-independent dissipation described by a series resistance g_e and (2) a frequency-dependent dissipation due to AC puddle transport, modeled by the parameters c_p, g_p, and f_p. As the temperature or excitation voltage increases, the dissipation is modified by the increased contribution of bulk carriers due to thermal excitation or breakdown and percolation through the bulk [15]. This statement is substantiated by Fig. 4, showing the fit parameters at various excitation voltages U. We observe a coupling capacitance C_g enhanced by nearly 1 order of magnitude from 4 fF at 10 μV to 35 fF at 2 mV, while g_e increases. In the meantime, the puddle capacitance c_p drops from approximately $235\,\text{pF}\,\text{m}^{-1}$ to approximately $100\,\text{pF}\,\text{m}^{-1}$. Both features indicate a more metallic bulk with increased dissipation due to the activation of bulk carriers and result in an increased velocity by roughly a factor of 2 from 160 to $390\,\text{km}\,\text{s}^{-1}$. This reduced velocity at low excitation voltage approaches the universal value recently predicted [33], $v = \frac{1}{2\sqrt{2}R_K\epsilon} \simeq 160\text{–}220\,\text{km}\,\text{s}^{-1}$, with $\epsilon \simeq 7\epsilon_0\text{–}10\epsilon_0$ being the average surrounding dielectric constant. However, the adverse roles of puddles and Coulomb interaction (not taken into account here) could interplay in reaching this value. The characteristic puddle frequency f_p shows a maximum of 8.5 GHz at $U \simeq 60\,\mu\text{V}$.

We also emphasize that the crossover between these two distinct low- and high-voltage regimes occurs for an excitation energy scale $eU \simeq 60\,\mu\text{eV}$. This agrees well with activation energies found in DC experiments [4,6,15,34,35]. As seen above, edge state transport is broken by an excitation voltage and higher temperature T, typically at the onset of bulk conductivity at approximately $T = 200\,\text{mK}$. This provides the means to investigate the relation between the rf bulk conductance g_e and the longitudinal resistance r_{xx} independently measured in DC. To correct for errors in the amplitude calibration, we focus on the relative variation $\Delta g_e(T) = g_e(T) - g_e(T = 0)$ and compare it with the line conductance $g_{xx} \simeq r_{xx}/R_{yx}^2$ following the usual relations between conductivity and resistance in a Hall system, in the low-loss limit [36]. Figure 4(d) shows the temperature dependence of g_e and g_{xx}, which exhibit similar temperature dependence, namely, a strong increase from $g_e, g_{xx} < 0.05\,\text{S}\,\text{m}^{-1}$ at low T to larger values $> 0.5\,\text{S}\,\text{m}^{-1}$ for $T > 1\,\text{K}$. The change in g_e and g_{xx} is well fitted by the variable-range-hopping model $g(T) = g_0 \exp[-(T_0/T)^{1/2}]/T$ describing disordered systems at low temperature for $T_0 \simeq 16\,\text{K}$. This behavior, observed in all devices, strongly supports a common origin, namely, the bulk conductivity, as the source of the frequency-independent dissipation. The fit values for T_0 and f_p are comparable to those observed in Cr-BST [16] but an order of magnitude lower than those in graphene [27], indicating a much stronger disorder. In addition, we also observed an enhanced velocity (low puddle capacitance c_p) and coupling for larger temperatures [see Fig. 4(c)], confirming a metallic behavior at higher temperatures, as already observed for large excitation voltages.

Summary and conclusions. In summary, we reported on the measurement of edge plasmon characteristics in the QAH state of V-BST using broadband microwave transport. In the low-voltage and low-temperature regime necessary to observe a robust QAH state, we found a velocity $v \simeq 200\,\text{km}\,\text{s}^{-1}$, close to the universal value calculated from a noninteracting, disorder-free theory [33]. This velocity increases as higher excitation voltages or temperatures progressively destroy the QAH state, with values close to those observed in Cr-doped $(\text{Bi}_x\text{Sb}_{1-x})_2\text{Te}_3$ [9,16]. Dissipation is mostly dominated by frequency-dependent losses in the low-voltage, low-temperature regime, which we ascribe to charge puddles and model as an *RC* series circuit. When the QAH state breaks down under increased temperature or excitation voltage, the dissipation rapidly becomes dominated by a frequency-independent mechanism, which we relate to the residual longitudinal resistance measured in DC transport experiments. Edge states coupled to puddles exhibit larger widths [20,26]. Recent observations of several micron-wide

edge states via microwave impedance microscopy [37] in V-doped BST align well with this interpretation. This work primarily confirms the propagation of QAH edge plasmons at large distances and high frequencies, here up to 100 μm and 4 GHz, making it a promising platform for plasmonics. It is an important step towards the realization and improvement of QAH-based nonreciprocal components [8,9] and towards the generation of flying Majorana anyons [11]. As a result of the quantitative studies of the devices, we predict that, under the best conditions, circulators and resonators [38] based on the measured thin films could reach quality factors approaching 100 at a few tens of megahertz. Future work will aim to clarify the role of screening gates [17]. The present work also indicates the prominent role of puddles in the dissipation and likely in the breakdown of the quantum anomalous Hall effect. Using microwave signals as probes, future research will investigate the breakdown dynamics.

The supporting data and codes for this article are available from Zenodo [39].

Acknowledgments. The authors warmly thank C. Dickel, J. Hemberger, M. Hashisaka, N. Kumada, H. Kamata, G. Fève, E. Frigerio, and G. Ménard for insightful discussions. This work was supported by the ERC, under Contract No. ERC-2017-STG-758077 "CASTLES"; Germany's Excellence Strategy (Cluster of Excellence Matter and Light for Quantum Computing ML4Q, EXC 2004/1-390534769); and the DFG (SFB1238 Control and Dynamics of Quantum Materials, 277146847, Projects No. A04 and No. B07).

[1] C.-Z. Chang *et al.*, Experimental observation of the quantum anomalous Hall effect in a magnetic topological insulator, Science **340**, 167 (2013).

[2] C.-Z. Chang, W. Zhao, D. Y. Kim, H. Zhang, B. A. Assaf, D. Heiman, S.-C. Zhang, C. Liu, M. H. W. Chan, and J. S. Moodera, High-precision realization of robust quantum anomalous Hall state in a hard ferromagnetic topological insulator, Nat. Mater. **14**, 473 (2015).

[3] R. Yu, W. Zhang, H.-J. Zhang, S.-C. Zhang, X. Dai, and Z. Fang, Quantized anomalous Hall effect in magnetic topological insulators, Science **329**, 61 (2010).

[4] A. J. Bestwick, E. J. Fox, X. Kou, L. Pan, K. L. Wang, and D. Goldhaber-Gordon, Precise quantization of the anomalous Hall effect near zero magnetic field, Phys. Rev. Lett. **114**, 187201 (2015).

[5] M. Götz, K. M. Fijalkowski, E. Pesel, M. Hartl, S. Schreyeck, M. Winnerlein, S. Grauer, H. Scherer, K. Brunner, C. Gould, F. J. Ahlers, and L. W. Molenkamp, Precision measurement of the quantized anomalous Hall resistance at zero magnetic field, Appl. Phys. Lett. **112**, 072102 (2018).

[6] E. J. Fox, I. T. Rosen, Y. Yang, G. R. Jones, R. E. Elmquist, X. Kou, L. Pan, K. L. Wang, and D. Goldhaber-Gordon, Part-per-million quantization and current-induced breakdown of the quantum anomalous Hall effect, Phys. Rev. B **98**, 075145 (2018).

[7] K. M. Fijalkowski, N. Liu, M. Klement, S. Schreyeck, K. Brunner, C. Gould, and L. W. Molenkamp, A balanced quantum Hall resistor, Nat. Electron. **7**, 438 (2024).

[8] G. Viola and D. P. DiVincenzo, Hall effect gyrators and circulators, Phys. Rev. X **4**, 021019 (2014).

[9] A. C. Mahoney, J. I. Colless, L. Peeters, S. J. Pauka, E. J. Fox, X. Kou, L. Pan, K. L. Wang, D. Goldhaber-Gordon, and D. J. Reilly, Zero-field edge plasmons in a magnetic topological insulator, Nat. Commun. **8**, 1836 (2017).

[10] A. Uday, G. Lippertz, K. Moors, H. Legg, A. Bliesener, L. Pereira, A. Taskin, and Y. Ando, Induced superconducting correlations in a quantum anomalous Hall insulator, Nat. Phys. **8**, 1836 (2024).

[11] C. W. J. Beenakker, P. Baireuther, Y. Herasymenko, I. Adagideli, L. Wang, and A. R. Akhmerov, Deterministic creation and braiding of chiral edge vortices, Phys. Rev. Lett. **122**, 146803 (2019).

[12] C. Beenakker, A. Grabsch, and Y. Herasymenko, Electrical detection of the Majorana fusion rule for chiral edge vortices in a topological superconductor, SciPost Phys. **6**, 022 (2019).

[13] G. M. Ferguson, R. Xiao, A. R. Richardella, D. Low, N. Samarth, and K. C. Nowack, Direct visualization of electronic transport in a quantum anomalous Hall insulator, Nat. Mater. **22**, 1100 (2023).

[14] S. Komiyama and Y. Kawaguchi, Heat instability of quantum Hall conductors, Phys. Rev. B **61**, 2014 (2000).

[15] G. Lippertz, A. Bliesener, A. Uday, L. M. C. Pereira, A. A. Taskin, and Y. Ando, Current-induced breakdown of the quantum anomalous Hall effect, Phys. Rev. B **106**, 045419 (2022).

[16] L. A. Martinez, G. Qiu, P. Deng, P. Zhang, K. G. Ray, L. Tai, M.-T. Wei, H. He, K. L. Wang, J. L. DuBois, and D.-X. Qu, Edge magnetoplasmon dispersion and time-resolved plasmon transport in a quantum anomalous Hall insulator, Phys. Rev. Res. **6**, 013081 (2024).

[17] N. Kumada, N.-H. Tu, K.-I. Sasaki, T. Ota, M. Hashisaka, S. Sasaki, K. Onomitsu, and K. Muraki, Suppression of gate screening on edge magnetoplasmons by highly resistive ZnO gate, Phys. Rev. B **101**, 205205 (2020).

[18] See Supplemental Material at http://link.aps.org/supplemental/10.1103/PhysRevB.110.L161403 for information about the sample preparation, the rf setup and its calibration, the circuit model, the fitting of the data, and the results of other samples, which includes Refs. [9,16,20].

[19] K. M. Fijalkowski, N. Liu, P. Mandal, S. Schreyeck, K. Brunner, C. Gould, and L. W. Molenkamp, Quantum anomalous Hall edge channels survive up to the Curie temperature, Nat. Commun. **12**, 5599 (2021).

[20] A. Gourmelon, E. Frigerio, H. Kamata, L. Lunczer, A. Denis, P. Morfin, M. Rosticher, J.-M. Berroir, G. Fève, B. Plaçais, H. Buhmann, L. W. Molenkamp, and E. Bocquillon, Velocity and confinement of edge plasmons in HgTe-based two-dimensional topological insulators, Phys. Rev. B **108**, 035405 (2023).

[21] C. Jozwiak, J. A. Sobota, K. Gotlieb, A. F. Kemper, C. R. Rotundu, R. J. Birgeneau, Z. Hussain, D.-H. Lee, Z.-X. Shen, and A. Lanzara, Spin-polarized surface resonances accompanying topological surface state formation, Nat. Commun. **7**, 13143 (2016).

[22] Y. L. Chen, J.-H. Chu, J. G. Analytis, Z. K. Liu, K. Igarashi, H.-H. Kuo, X. L. Qi, S. K. Mo, R. G. Moore, D. H. Lu, M.

Hashimoto, T. Sasagawa, S. C. Zhang, I. R. Fisher, Z. Hussain, and Z. X. Shen, Massive Dirac fermion on the surface of a magnetically doped topological insulator, Science **329**, 659 (2010).

[23] N. Kumada, H. Kamata, and T. Fujisawa, Edge magnetoplasmon transport in gated and ungated quantum Hall systems, Phys. Rev. B **84**, 045314 (2011).

[24] C. de C. Chamon and X. G. Wen, Sharp and smooth boundaries of quantum Hall liquids, Phys. Rev. B **49**, 8227 (1994).

[25] D. B. Chklovskii, B. I. Shklovskii, and L. I. Glazman, Electrostatics of edge channels, Phys. Rev. B **46**, 4026 (1992).

[26] H. Kamata, H. Irie, N. Kumada, and K. Muraki, Time-resolved measurement of ambipolar edge magnetoplasmon transport in InAs/InGaSb composite quantum wells, Phys. Rev. Res. **4**, 033214 (2022).

[27] N. Kumada, P. Roulleau, B. Roche, M. Hashisaka, H. Hibino, I. Petkovic, and D. C. Glattli, Resonant edge magnetoplasmons and their decay in graphene, Phys. Rev. Lett. **113**, 266601 (2014).

[28] A. Gourmelon, H. Kamata, J.-M. Berroir, G. Fève, B. Plaçais, and E. Bocquillon, Characterization of helical Luttinger liquids in microwave stepped-impedance edge resonators, Phys. Rev. Res. **2**, 043383 (2020).

[29] M. C. Dartiailh, S. Hartinger, A. Gourmelon, K. Bendias, H. Bartolomei, H. Kamata, J.-M. Berroir, G. Fève, B. Plaçais, L. Lunczer, R. Schlereth, H. Buhmann, L. W. Molenkamp, and E. Bocquillon, Dynamical separation of bulk and edge transport in HgTe-based 2D topological insulators, Phys. Rev. Lett. **124**, 076802 (2020).

[30] A. Inhofer, J. Duffy, M. Boukhicha, E. Bocquillon, J. Palomo, K. Watanabe, T. Taniguchi, I. Estève, J. M. Berroir, G. Fève, B. Plaçais, and B. A. Assaf, rf quantum capacitance of the topological insulator Bi_2Se_3 in the bulk depleted regime for field-effect transistors, Phys. Rev. Appl. **9**, 024022 (2018).

[31] C. Lin, M. Hashisaka, T. Akiho, K. Muraki, and T. Fujisawa, Time-resolved investigation of plasmon mode along interface channels in integer and fractional quantum Hall regimes, Phys. Rev. B **104**, 125304 (2021).

[32] M. Bagchi, L. Pitz-Paal, C. P. Grams, O. Breunig, N. Borgwardt, Z. Wang, Y. Ando, M. Grüninger, and J. Hemberger, Large positive magnetoconductivity at microwave frequencies in the compensated topological insulator $BiSbTeSe_2$, Phys. Rev. B **99**, 161121(R) (2019).

[33] F. Zhang, C. Ding, J. Zhou, and Y. Yao, Chiral edge plasmons in quantum anomalous Hall insulators, arXiv:2404.13930.

[34] C.-Z. Chang, W. Zhao, D. Y. Kim, P. Wei, J. K. Jain, C. Liu, M. H. W. Chan, and J. S. Moodera, Zero-field dissipationless chiral edge transport and the nature of dissipation in the quantum anomalous Hall state, Phys. Rev. Lett. **115**, 057206 (2015).

[35] M. Kawamura, R. Yoshimi, A. Tsukazaki, K. S. Takahashi, M. Kawasaki, and Y. Tokura, Current-driven instability of the quantum anomalous Hall effect in ferromagnetic topological insulators, Phys. Rev. Lett. **119**, 016803 (2017).

[36] D. Yoshioka, *The Quantum Hall Effect* (Springer Verlag, Berlin, 2002).

[37] M. Allen, Y. T. Cui, E. Y. Ma, M. Mogi, M. Kawamura, I. C. Fulga, D. Goldhaber-Gordon, Y. Tokura, and Z. X. Shen, Visualization of an axion insulating state at the transition between 2 chiral quantum anomalous Hall states, Proc. Natl. Acad. Sci. USA **116**, 14511 (2019).

[38] E. Frigerio, G. Rebora, M. Ruelle, H. Souquet-Basiège, Y. Jin, U. Gennser, A. Cavanna, B. Plaçais, E. Baudin, J. M. Berroir, I. Safi, P. Degiovanni, G. Fève, and G. Ménard, Gate tunable edge magnetoplasmon resonators, Commun. Phys. **7**, 314 (2024).

[39] T. Röper and E. Bocquillon, Propagation, dissipation and breakdown in quantum anomalous Hall edge states probed by microwave edge plasmons, Zenodo (2024), doi:10.5281/zenodo.11344274.